CrystEngComm

ROYAL SOCIETY OF CHEMISTRY

PAPER

View Article Online
View Journal | View Issue

Cite this: *CrystEngComm*, 2020, **22**, 4250

In situ coupling of TiO_2(B) and ZIF-8 with enhanced photocatalytic activity *via* effective defect†

Xiaoxue Qi,[a] Feng Shang,[b] Tao Wang,[c] Yuqin Ma *[a] and Yongsheng Yan *[cd]

Received 20th April 2020,
Accepted 25th May 2020

DOI: 10.1039/d0ce00595a

rsc.li/crystengcomm

In recent years, photocatalytic degradation on inorganic semiconductors has been attracting widespread attention. However, for a single semiconductor, the speed of the recombination of electrons and holes is fast, which leads to a decrease in the absorption of sunlight, thereby affecting its photocatalytic efficiency. Therefore, the coupling of semiconductor and metal–organic framework is of great significance due to its porosity and large specific surface area. Herein, a composite photocatalyst was obtained by coupling ZIF-8 and TiO_2(B) *via* a simple method. XRD, FT-IR spectroscopy, SEM, TEM, UV-visible diffuse reflectance spectroscopy, XPS, EPR and EDS were used to study the as-prepared samples. Photocatalytic degradation experiments confirmed that the composites have significantly improved photodegradation performance due to the increased light utilization and fast charge carrier transfer. Moreover, the possible mechanism of photodegradation was also proposed. This study provides an initial view on the coupling of semiconductor and metal–organic framework to enhance the photocatalytic performance.

1. Introduction

Environmental hazards and energy problems are the two major issues that have arisen along with the rapid development of industries, and have become the key challenges that mankind urgently needs to solve.[1,2] Photocatalysis, a new and effective green process, converts light energy into chemical energy to provide the energy needed for reactions and oxidizes nearby water molecules and oxygen into free anions during the catalysis. Therefore, it has immeasurable application prospects in the field of environmental protection and energy utilization. Unfortunately, the development of photocatalysts limits the development of the photocatalytic technology.

Semiconductor materials are currently the most widely used photocatalysts, including oxides (TiO_2,[3] ZnO,[4] Fe_2O_3,[5] *etc.*), sulfides (ZnS,[6] CdS,[7] CuS,[8] *etc.*), and novel photocatalysts (g-C_3N_4,[9,10] $ATiO_3$,[11] molecular sieve,[12] *etc.*).[13] With the growth of research on photocatalysts, the application range of the photocatalytic technology has broadened, which can not only be used to degrade organic pollutants in wastewater into water and CO_2 but also further transform water into clean H_2 energy. Therefore, research on semiconductor photocatalysts is of great significance.[14]

TiO_2 has been the most important photocatalyst in the past few decades due to its excellent chemical stability, thermal stability, good dispersibility, non-toxicity and low cost.[15] However, due to its slight wide band gap and the fast recombination of electrons and holes, its practical

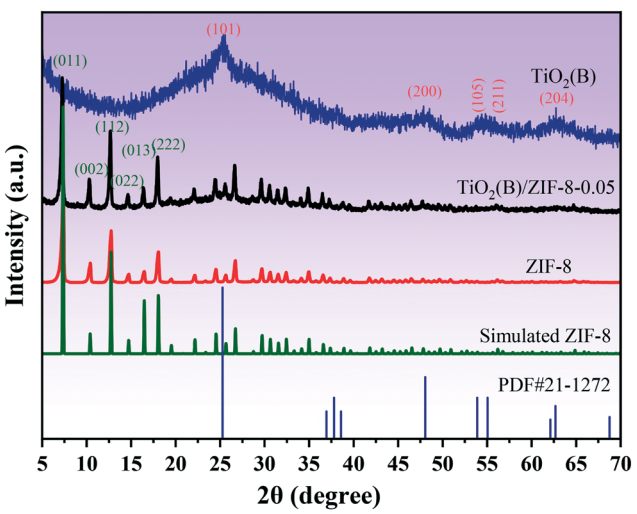

Fig. 1 XRD patterns of TiO_2(B), ZIF-8, and TiO_2(B)/ZIF-8.

[a] *School of Chemistry and Environmental Engineering, Changchun University of Science and Technology, 86-130022 Changchun, Jilin Province, P. R. China. E-mail: myq3939@163.com; Tel: +15044087078*
[b] *Bureau of Ecology and Environment of Changchun Jiutai Branch Office, 130022 Changchun, P. R. China*
[c] *School of Chemistry and Chemical Engineering, Jiangsu University, 212013 Zhenjiang, P. R. China*
[d] *Institute of Green Chemistry and Chemical Technology, Jiangsu University, 212013 Zhenjiang, P. R. China*

† Electronic supplementary information (ESI) available. See DOI: 10.1039/d0ce00595a

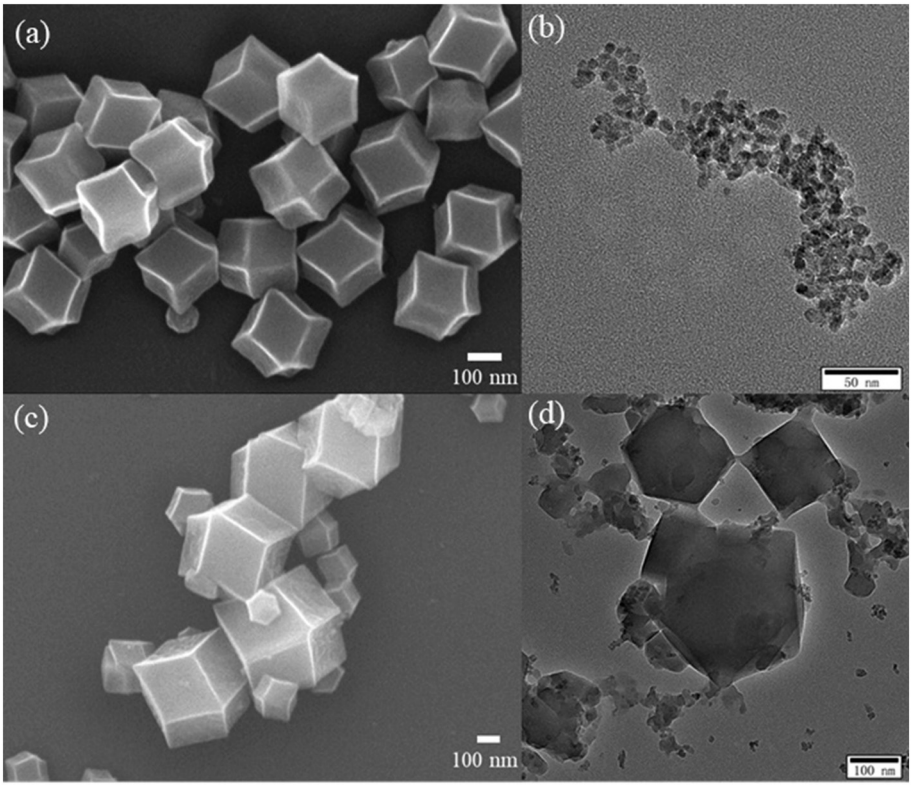

Fig. 2 SEM image of ZIF-8 (a) and TEM image of TiO_2(B) (b), SEM and TEM images of TiO_2(B)/ZIF-8 (c and d).

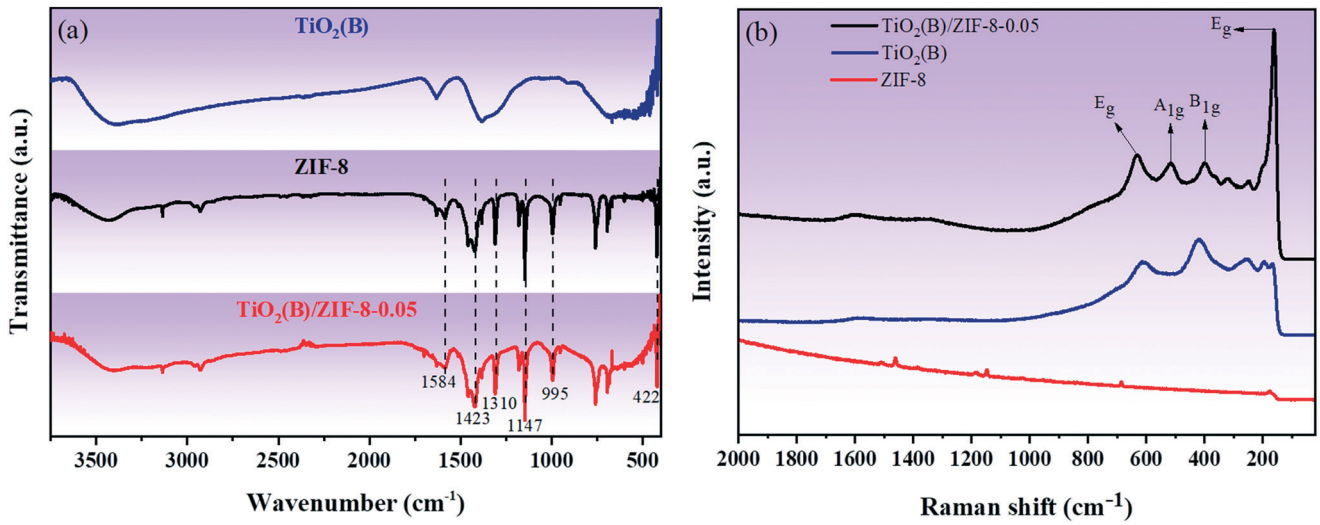

Fig. 3 (a) FT-IR spectra of TiO_2(B), TiO_2(B)/ZIF-8 and ZIF-8; (b) characteristic Raman spectra of TiO_2(B), ZIF-8 and TiO_2(B)/ZIF-8.

applications are limited.[16–19] In order to broaden the application of TiO_2, numerous methods, including metal and non-metal doping, band gap engineering, semiconductor coupling, morphology tuning and heterojunction fabrication, have been studied to improve the shortcomings of TiO_2.[1,20] Among them, semiconductor coupling is the common and efficient way to make the effective use of sunlight and improve the light stability of TiO_2.

Metal–organic frameworks (MOFs) are a class of multifunctional materials with repeated network structure formed *via* the self-assembly of organic ligands and metal ions. Because of their porosity, large specific surface area, and unsaturated metal site, MOFs and composite MOF materials have/application prospects in the catalytic applications.[21–24] Therefore, continuing research and development on the multi-functional MOFs and composite MOF materials and application in different fields will greatly promote the mutual development of the disciplines.[25–28] Among them, ZIF-8 is a simple and easy-to-synthesize porous material that combines the high stability of inorganic zeolites

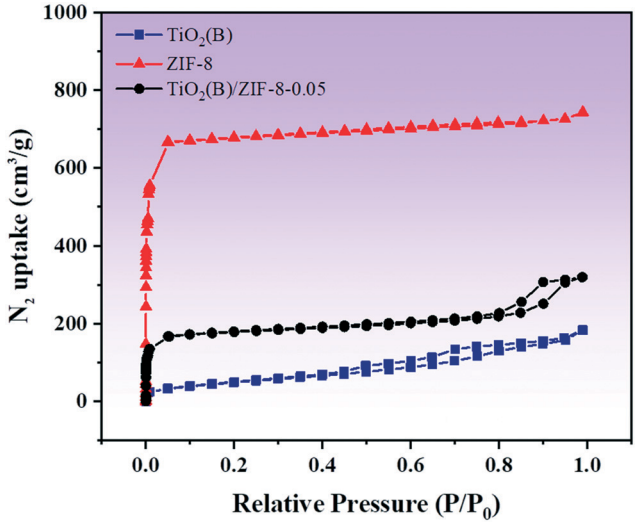

Fig. 4 N_2 adsorption isotherms measured at 77 K.

Table 1 Physical properties of sample

Samples	BET ($m^2\ g^{-1}$)	Pore volume ($cm^3\ g^{-1}$)	Pore width (nm)
TiO_2(B)	179.3	0.25	7.8
ZIF-8	2831.8	1.05	1.7
TiO_2(B)/ZIF-8	710.5	0.46	5.0

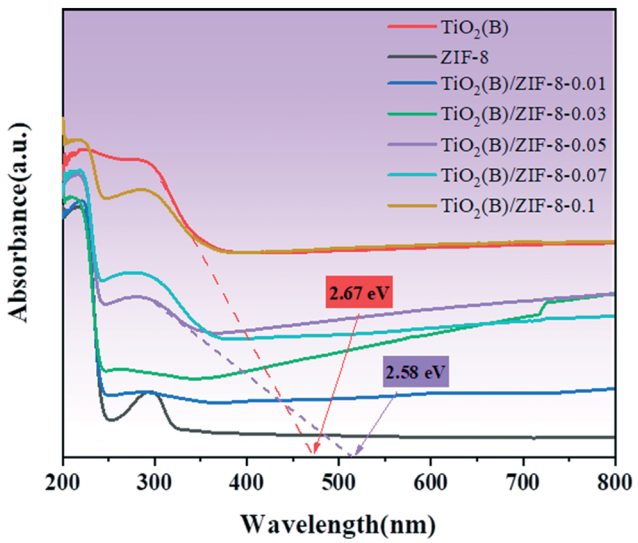

Fig. 5 UV-vis diffuse reflectance spectra of different samples.

with the high porosity and organic function of MOFs, making it one of the most popular metal–organic frameworks.[29,30]

To date, numerous studies have been conducted to combine ZIF-8 and semiconductor to prepare a composite catalyst with higher catalytic efficiency. Li *et al.* reported the successful loading of CoB onto ZIF-8 *via* a one-step reduction method and examined its activity in the hydrogen production.[31] Zhang *et al.* successfully synthesized TiO_2@ZIF-8 hollow nanospheres with a double-shell structure by ultrasonic crystallization for photocatalytic hydrogen evolution.[14] Pipelzadeh *et al.* prepared a new ZIF-8/TiO_2 nanocomposite for the photocatalytic reduction of CO_2 to CH_4 and CO.[32] As expected, by combining ZIF-8 and TiO_2, the photocatalytic activity was greatly improved. Recently, a black TiO_2 (TiO_2(B)) has been reported and attracted considerable attention. Mao *et al.* proposed black TiO_2 and found that black TiO_2 has stronger absorption of sunlight than white TiO_2.[33] Ye *et al.* reported nickel-loaded black TiO_2 with an inverse opal structure and used for the stable and efficient reduction of CO_2.[20] Therefore, it was meaningful to explore the photocatalytic activity of the TiO_2(B)/ZIF-8 composite.

Unlike Zhang and Li who used pure TiO_2 and ZIF-8 for coupling, in this study, we prepared a composite catalyst with high catalytic efficiency by coupling black TiO_2 and ZIF-8. XRD, EDS, SEM and TEM analyses confirmed the successful combination of TiO_2(B) and ZIF-8. Based on the results of Raman, UV-vis diffuse reflectance, EPR and XPS, it is proposed that the improvement of the photocatalytic activity was due to the generation of oxygen vacancies and Ti^{3+}. Furthermore, the photocatalytic degradation mechanism of TC is also discussed. This study provides important roadmap for the continuous exploration of the application of MOF-based semiconductor composites in photocatalysis and environmental protection.

2. Experimental

2.1. Materials

All the chemicals used during the experiment did not require further purification, and deionized water was used throughout the experiment. Tetrabutyltitanate ($C_{16}H_{36}O_4Ti$), sodium borohydride ($NaBH_4$, ≥98%), zinc nitrate hexahydrate ($Zn(NO_3)_2{\cdot}6H_2O$, ≥99.0%), absolute ethanol (CH_3CH_2OH, ≥99.7%), methanol (CH_4O, ≥99.5%), citric acid ($C_6H_8O_7$, ≥99.7%), ascorbic acid ($C_6H_8O_6$, ≥99.7%), and isopropyl alcohol (C_3H_8O, ≥99.7%) were purchased from Sinopharm Chemical Reagent Co. 2-Methylimidazole ($C_4H_6N_2$, ≥98%) was purchased from Aladdin Industrial Corporation.

2.2. Preparation of black TiO_2

Black TiO_2 was prepared according to the previously reported procedure.[3] 3.0 mL of tetrabutyltitanate was added to a beaker containing 50 mL of deionized water. After stirring for 30 min, the mixture was poured into the reaction vessel and reacted at 180 °C for 6 h. Then, the obtained sample was centrifuged, washed 4 to 5 times with deionized water and ethanol, and dried in an oven at 60 °C to obtain white TiO_2. Furthermore, 1.0 g of white TiO_2 and 2.0 g of sodium borohydride were mixed and ground evenly. Then, the mixture was put into a tube furnace and calcined at 350 °C for 1 h at a heating rate of 5 °C min^{-1}. After the temperature was naturally cooled, the calcined powder was washed for at least 5 to 6 times with deionized water until the final washing liquid became neutral, followed by drying in an oven at 60 °C to obtain black TiO_2.

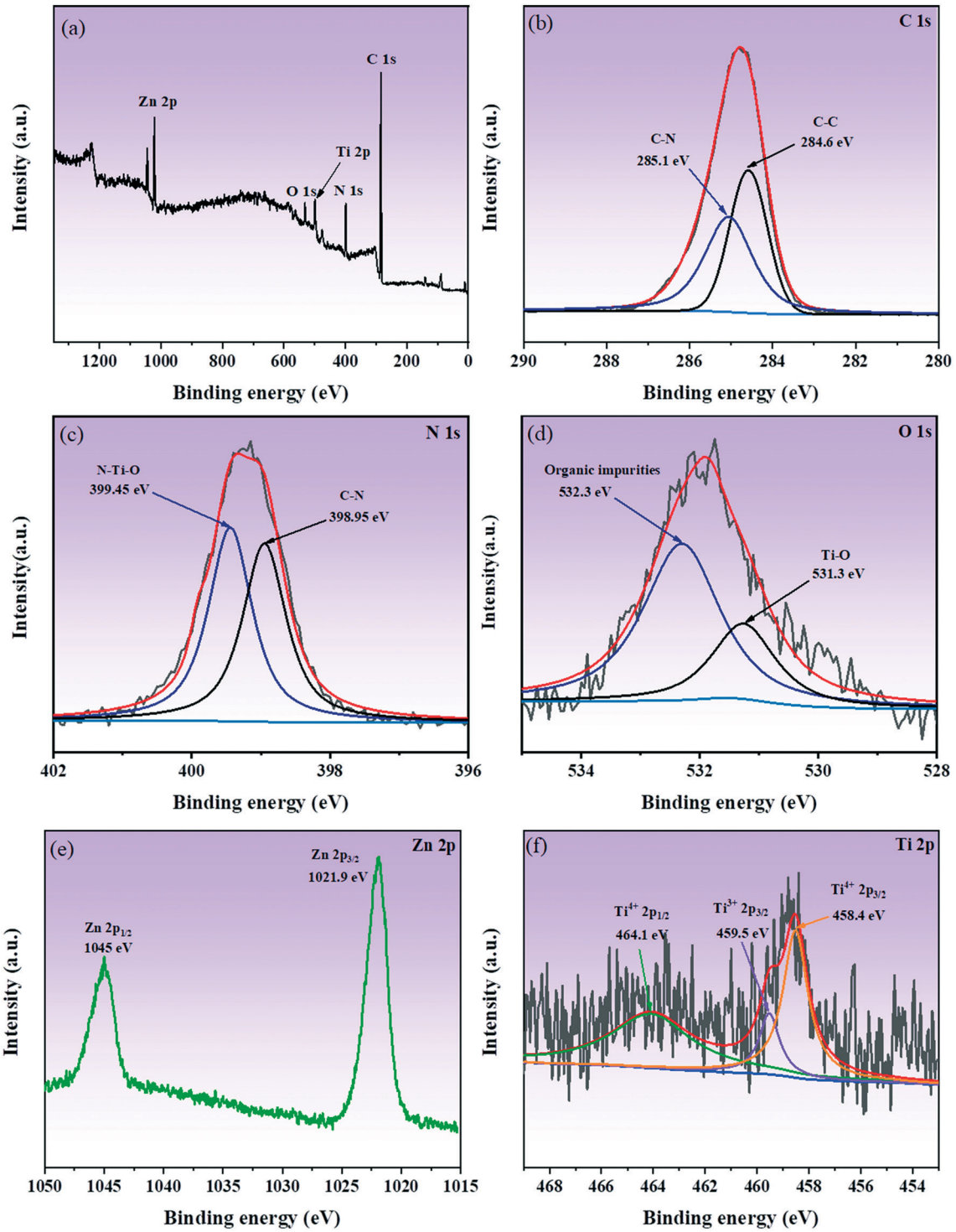

Fig. 6 XPS survey spectrum of TiO_2(B)/ZIF-8 (a); high-resolution XPS spectrum of C 1s, Zn 2p, N 1s, Ti 2p, and O 1s (b–f).

2.3. Synthesis of the TiO_2(B)/ZIF-8 composite

TiO_2(B)/ZIF-8 composite was prepared *via* a simple method. 0.7437 g of zinc nitrate hexahydrate and 0.4105 g of 2-methylimidazole were dissolved in 50 mL of methanol, and labeled as solution A and solution B, respectively. Then, 0.03 g of black TiO_2 was dissolved in solution A and ultrasonically dispersed. Thereafter, the solutions A and B were mixed with mechanical stirring at 50 °C for 1 h. The mixture was then centrifuged and washed 4 times with methanol and dried in a vacuum oven at 80 °C. Moreover, different addition amounts of TiO_2(B) in the composite (0 g, 0.01 g, 0.03 g, 0.07 g, and 0.1 g) were obtained under identical conditions. Pure ZIF-8 was obtained in the absence of TiO_2(B) (0 g), and the

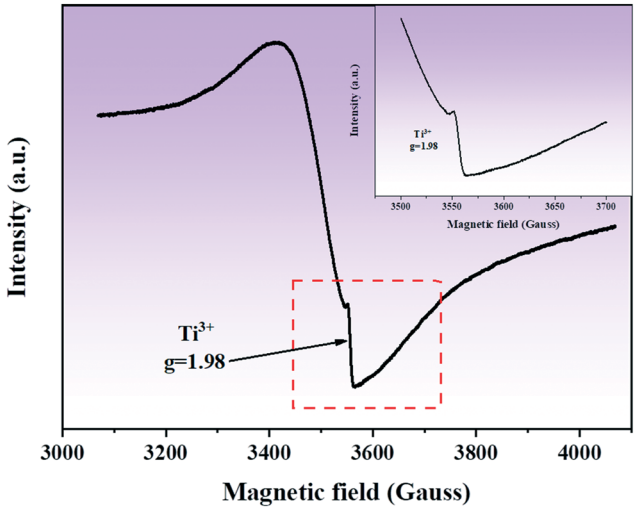

Fig. 7 EPR spectra of TiO_2(B)/ZIF-8.

obtained composites were labeled as TiO_2(B)/ZIF-8-x (x is the amount of TiO_2(B)).

2.4. Photocatalytic experiments

10 mg of the catalyst was dispersed in 100 mL solution containing 10 mg L^{-1} tetracycline, and stirred under dark conditions for 30 min to achieve an adsorption–desorption balance. Then, the visible light source was turned on to start the degradation experiment, and cold water was circulated to keep the reaction at normal temperature. The samples were taken every 15 min and centrifuged for the removal of the solid catalyst. The filtrate was measured by the UV-vis absorption spectroscopy and analyzed based on the change of the concentration of tetracycline recorded by its absorbance.[3,14,34]

2.5. Free radical scavenging test

To determine the role of the reactive substances in the photodegradation of tetracycline, the free radical scavenging experiments were carried out. The effects of holes, hydroxyl radicals and superoxide radicals on the photodegradation were studied using citric acid, ascorbic acid and iso-propyl alcohol, respectively. A certain amount of the scavenger was added in each experiment, keeping the experimental conditions the same as the previous photocatalytic experiments.[35]

3. Results and discussion

XRD was used to analyze the crystal structure of the as-prepared sample. Fig. 1 shows the XRD patterns of the TiO_2(B), ZIF-8, and TiO_2(B)/ZIF-8 composites. The characteristic peaks of TiO_2(B) were observed at 25.36°, 47.86°, 53.96°, 55.86°, and 62.74°, which were attributed to the (101), (200), (105), (211), and (204) crystal planes of TiO_2 (PDF# 71-1167), respectively.[3] According to the ZIF-8 simulated card, it can be seen that the as-prepared sample exhibited the characteristic peaks at 7.26°, 10.3°, 12.6°, 14.68°, 16.4°, 18.0° which were attributed to the (011), (002), (112), (022), (013) and (222) crystal planes of ZIF-8, and were consistent with the previous reports.[14,30] For the composite TiO_2(B)/ZIF-8, the XRD pattern shows all the characteristic diffraction peaks of ZIF-8, without any clear characteristic peak of TiO_2(B) due to the weak peak intensity of the nanosized TiO_2(B). SEM and TEM were further used to prove the XRD results.

The morphology and size of the samples were analyzed *via* SEM and TEM. The SEM image of ZIF-8 is shown in Fig. 2a; its shape was a regular dodecahedron with uniform size and distribution. Fig. 2b shows the TEM image of TiO_2(B), which can be found to be about 10 nm in size, conforming to the

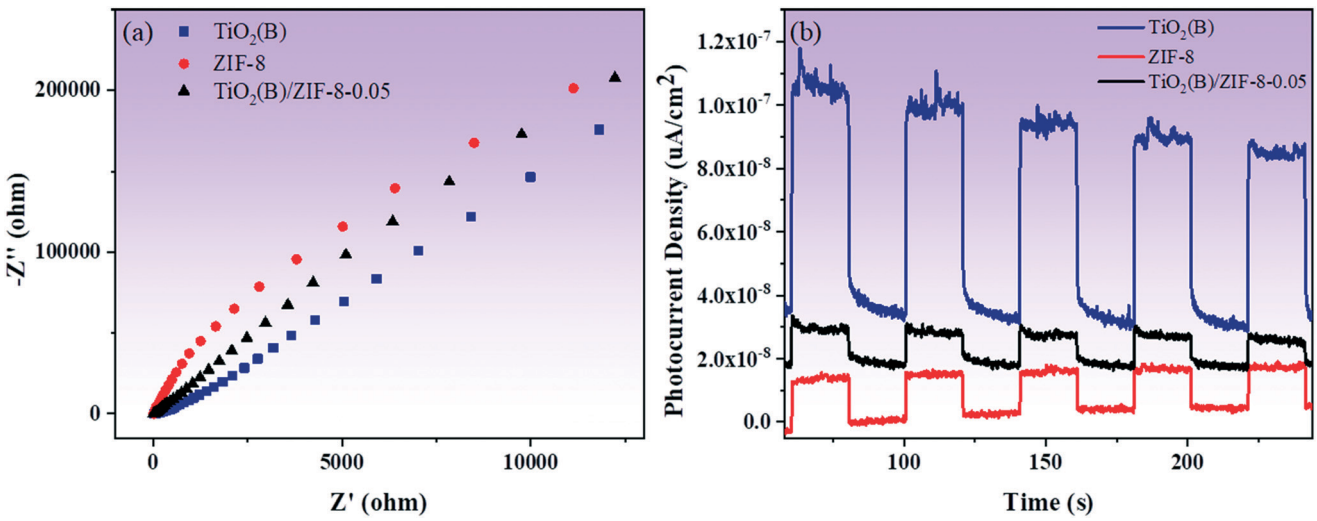

Fig. 8 Electrochemical impedance spectra (a) and photocurrent intensity (b) of TiO_2(B), ZIF-8 and TiO_2(B)/ZIF-8, respectively.

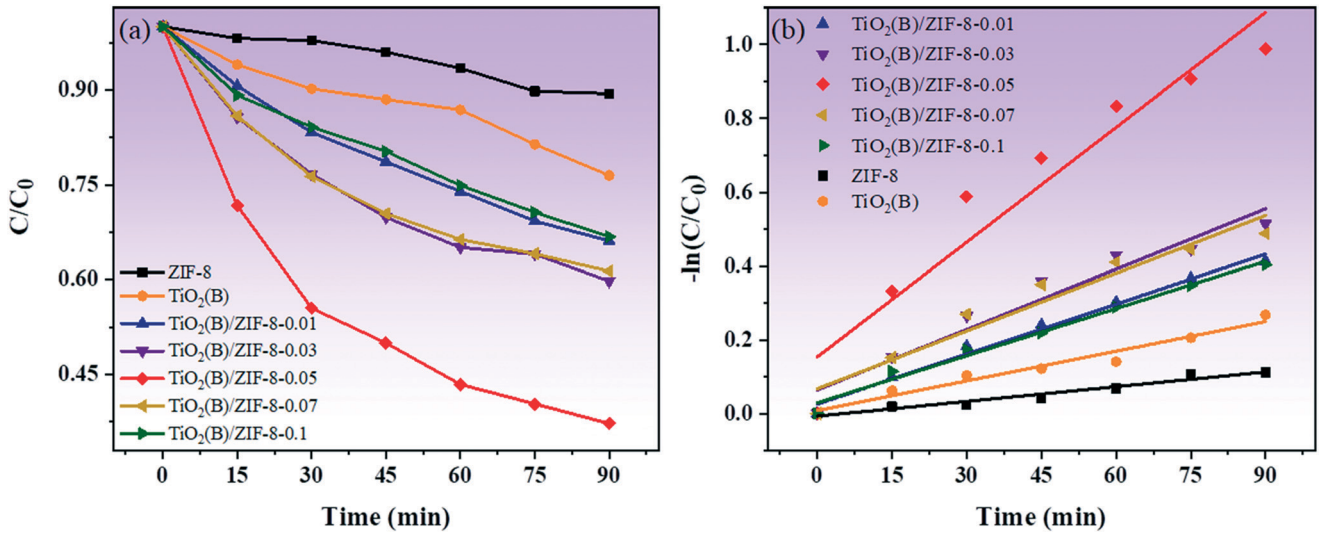

Fig. 9 Photocatalytic degradation of TC under visible light (a), plot of $-\ln(C/C_0)$ *versus* irradiation time for the degradation of TC (b).

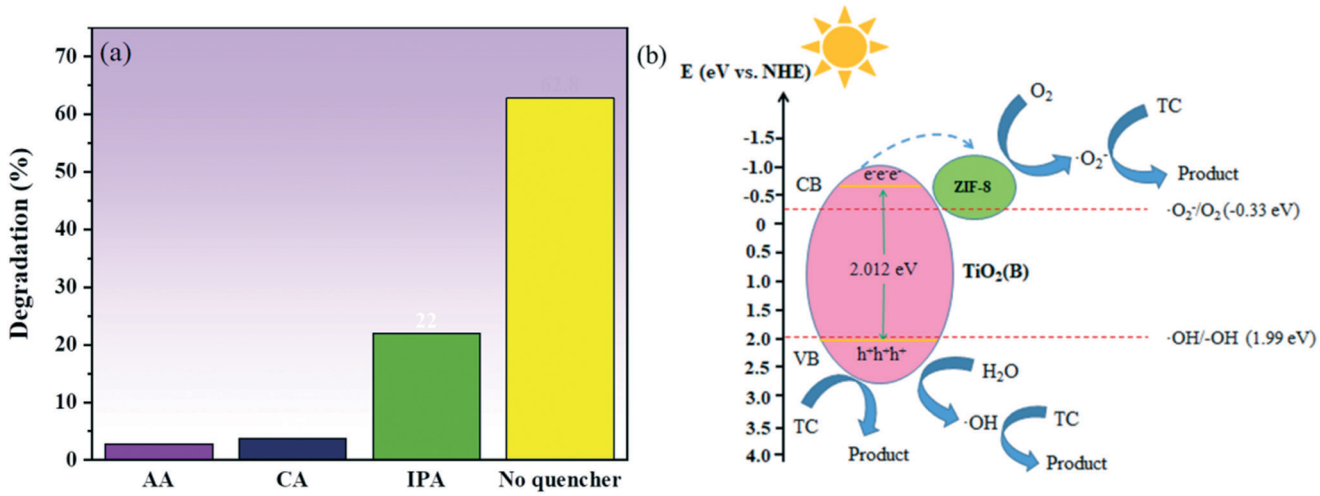

Fig. 10 The photocatalytic activity of TiO_2(B)/ZIF-8 composites and the degradation of TC by different quenchers under visible light (a), the photocatalytic degradation mechanism of the TiO_2(B)/ZIF-8 composite under visible light (b).

conjecture proposed *via* XRD. Fig. 2c displays the SEM image of the TiO_2(B)/ZIF-8 composite, which indicates that the crystal structure of ZIF-8 was not destroyed after combination with TiO_2(B), and the dodecahedral structure was maintained. No significant TiO_2(B) was observed in the SEM image due to the nanometer size of TiO_2(B), but it can be clearly seen in the TEM image (Fig. 2d) of the composite that TiO_2(B) was attached to the surface of ZIF-8. In addition, the elemental composition of the TiO_2(B)/ZIF-8 composite was determined *via* EDS. As shown in Fig. S1,† five elements (C, N, Ti, O and Zn) were detected in the composite, further indicating that the composite was successfully synthesized.[30]

FTIR spectroscopy was performed to analyze the chemical bonds present on the samples. Fig. 3a shows the FT-IR spectra of TiO_2(B), ZIF-8 and TiO_2(B)/ZIF-8. The vibrational bands of the as-prepared ZIF-8 at 422 cm^{-1} and 1584 cm^{-1} were assigned to the Zn–N and C=N stretching vibrations, respectively. The peaks appearing at 1423 cm^{-1} and 995 cm^{-1} are due to the stretching vibrations of C–N, and the vibration bands at 1147 cm^{-1} and 1310 cm^{-1} were due to the bending vibration of imidazole.[14,29] These are the typical characteristics of ZIF-8. For pure TiO_2(B), the vibrational zone between 400–700 cm^{-1} is attributed to the typical Ti–O–Ti bond vibration and Ti–O stretching vibration mode. The hydroxyl group resulted in a peak at 1632 cm^{-1}, and the peak between 3400 and 3500 cm^{-1} was due to the physical absorption of water on the surface of TiO_2(B).[3] All the characteristic peaks of TiO_2(B) and ZIF-8 are present in the composite, indicating that the composite was successfully synthesized.[3,14,30,34] Fig. 3b shows the characteristic Raman spectra of TiO_2(B), ZIF-8 and TiO_2(B)/ZIF-8. The peaks at 685.46 cm^{-1} and 1000–1600 cm^{-1} in ZIF-8 are caused by the imidazole ring vibration, C–H sway, C5–N stretching vibration and C4–C5 stretching mode.[29] As shown by the Raman spectrum of TiO_2(B), the peaks at 161 cm^{-1} and 632 cm^{-1} belong to the E_g mode, and the peaks at 398 cm^{-1} and 516

cm^{-1} belong to the B_{1g} and A_{1g} modes, respectively. This was consistent with the crystal structure of TiO_2(B).[36] Compared to TiO_2(B), the TiO_2(B)/ZIF-8 composite has a slight redshift, which was caused by the decrease in the grain size and oxygen vacancies during the reaction.[14,34]

In order to characterize the porous structure and specific surface area of the as-prepared TiO_2(B), ZIF-8 and composite material TiO_2(B)/ZIF-8, nitrogen adsorption–desorption studies were performed. Fig. 4 shows the adsorption–desorption isotherm of the as-prepared sample. As shown in Fig. 4, the curve corresponding to ZIF-8 shows type I isotherm, indicating that it is microporous. The curve of TiO_2(B) is a type IV isotherm because TiO_2(B) generates voids during assembly, so it shows single-layer adsorption at a low pressure and multilayer adsorption at a high pressure.[29] The composite shows a type IV isotherm, indicating a mesoporous structure. The specific surface area, pore width and pore volume of all the samples are summarized in Table 1. Compared to that of TiO_2(B), the specific surface area of the composite material increases. This is because ZIF-8, as a metal–organic framework, can well-disperse TiO_2(B), allowing it to be evenly distributed around its framework. A large specific surface area means that more active sites will participate in the reaction, thereby improving the efficiency and speed of the photocatalytic degradation of the pollutants.

The light absorption ability of the samples was analyzed *via* UV-vis diffuse reflectance spectroscopy. In Fig. 5, it is observed that the absorption wavelength of ZIF-8 is at around 230 nm, which means that ZIF-8 can only respond to UV light. For TiO_2(B), its absorption in the visible region significantly enhanced compared to the white TiO_2 reported in the literature, which was due to the introduction of Ti^{3+} and oxygen vacancies.[15] When ZIF-8 and TiO_2(B) were combined, the TiO_2(B)/ZIF-8 composite exhibits a wider absorption edge that extends into the visible region. This was due to the close contact between ZIF-8 and TiO_2(B), which alters the light absorption capacity of the composite.[3,14] The band gap energies of TiO_2(B) and the TiO_2(B)/ZIF-8 composite are also displayed in Fig. 5. Compared to ZIF-8, the band gap of TiO_2(B) and all the composites were smaller. The broadened visible-light absorption would enhance the photodegradation properties of the TiO_2(B)/ZIF-8 composite.

To analyze the chemical bonds and elemental composition present on the surface of the samples, XPS study was carried out. Fig. 6a shows the XPS survey spectrum of the TiO_2(B)/ZIF-8 composite, confirming the presence of five elements, *i.e.*, N, Ti, C, O, and Zn, in the composite. In the spectrum of C 1s (Fig. 6b), the peaks at 284.6 eV and 285.1 eV are due to the C–C and C–N bonds, respectively.[14] As shown in Fig. 6c (N 1s), the peaks at 398.95 eV and 399.45 eV are attributed to the C–N bond and the N–Ti–O bond of the imidazole ring in ZIF-8. The N–Ti–O bond indicated that the N atoms in the imidazole ring replaced some O atoms on the TiO_2(B) producing oxygen vacancies, which was consistent with the Raman results.[14] It can be seen in Fig. 6d that the XPS spectrum of O 1s produces bumps at 531.3 eV and 532.3 eV due to the Ti–O bond and organic impurities, respectively.[37,38] Fig. 6e shows the XPS spectrum of Zn 2p, and the peaks at 1021.9 eV and 1045 eV are caused by Zn $2p_{3/2}$ and Zn $2p_{1/2}$, respectively.[31,39] From Fig. 6f (Ti 2p), it can be seen that the binding energies at 458.4 eV and 464.1 eV is ascribed to Ti^{4+} in TiO_2(B).[3,40] The peak at 459.5 eV was due to the low oxidation state (Ti^{3+}) in TiO_2(B).[41] Therefore, the above XPS measurement results further proved that the composite was successfully prepared and the presence of oxygen vacancies in the composite.

In order to detect Ti^{3+} and oxygen vacancies in the composite, EPR studies were conducted. Fig. 7 shows the EPR spectrum of the composite. It can be seen that in the EPR spectrum of the composite, a clear symmetric signal is detected at $g = 1.98$, which can be attributed to the formation of defects in the sample, such as oxygen vacancies.

Fig. 8a shows the results of electrochemical impedance spectroscopy (EIS) measurements of the three samples. Compared to ZIF-8, the TiO_2(B) and TiO_2(B)/ZIF-8 composites have smaller impedance arc radii, with TiO_2(B) being the smallest. The small arc radius can increase the electron transfer speed and further improve the photocatalytic activity of the TiO_2(B)/ZIF-8 composites. Fig. 8b displayed the photocurrent intensity of all the samples. Although TiO_2(B) has the smallest impedance arc radius and the strongest photocurrent, as shown in Fig. 8b, its photocurrent intensity will gradually decrease with time. The photocurrent intensity of the TiO_2(B)/ZIF-8 composite was almost constant, demonstrating that the composite has better stability than TiO_2(B).

Fig. 9a shows the photocatalytic degradation of TC in presence of different photocatalysts. For ZIF-8 and TiO_2(B), the concentration of TC decreased by only 10% and 22% after 90 min under visible light irradiation. Compared with ZIF-8 and TiO_2(B), all the composites have good degradation effects. Also, with the increase in the amount of TiO_2(B), the photodegradation effects of the composite material gets better and better. In particular, the degradation effect of the TiO_2(B)/ZIF-8-0.05 composite was found to be optimum, which was 8 times and 3.6 times higher than that of ZIF-8 and TiO_2(B), respectively. This is because ZIF-8 can disperse TiO_2(B) more uniformly, thereby allowing more active sites to participate in the photodegradation reaction. The deterioration of the photodegradation effect of the TiO_2(B)/ZIF-8-0.07 and TiO_2(B)/ZIF-8-0.1 composites is due to the excessive aggregation of TiO_2(B), which reduces the absorption of sunlight. As shown in Fig. 9b, the TiO_2(B)/ZIF-8-0.05 composite also has the highest apparent rate constant, indicating that the oxygen vacancies can promote electron transfer and further increase the speed of the photodegradation of the composite.

In order to study the role of holes (h^+), hydroxyl radical ($^{\bullet}OH$) and superoxide radicals ($O_2^{\bullet-}$) in the degradation of the pollutants, a series of free radical scavenging experiments were performed, and the results are shown in Fig. 10a. The

degradation of TC was observed to be significantly inhibited in the presence of AA and CA, and the degradation of TC was also found to be affected in the presence of IPA. These results indicated that the role of holes (h^+) and superoxide radical ($O_2^{\bullet-}$) was critical in the degradation of TC, with the hydroxyl group ($^{\bullet}OH$) playing a supporting role. In order to determine the energy band structure of TiO_2(B)/ZIF-8 in a better way, the flat band potential of TiO_2(B) was measured using a Mott–Schottky plot. As can be seen from Fig. S2,† TiO_2(B) is a typical n-type semiconductor, and the flat band potential of TiO_2(B) is −0.8 V (*vs.* SCE), thus the standard hydrogen electrode is −0.558 V (*vs.* NHE) *via* calculate.[42] According to previous studies, it can be concluded that the conduction band (CB) of the n-type semiconductor is 0.1–0.3 eV lower than of the flat band potential.[43,44] Therefore, the conduction band position of TiO_2(B) was −0.658 eV, and the valence band position was calculated to be 2.012 eV according to the band gap diagram of Fig. 5. According to the conduction band and valence band positions of TiO_2(B), the band structure of TiO_2(B) was obtained and a possible photocatalytic route was proposed. As can be seen from Fig. 10b, the electrons and holes are generated on TiO_2(B) under excitation by light. In addition, the electrons are transferred from the conduction band of TiO_2(B) to ZIF-8, and then O_2 was electronically oxidized to superoxide radicals ($O_2^{\bullet-}$) to decompose TC. Simultaneously, the holes (h^+) not only decompose TC but also oxidize water to hydroxyl groups ($^{\bullet}OH$) to decompose TC, which was consistent with the results of the capture experiments.

4. Conclusions

In summary, the TiO_2(B)/ZIF-8 composite was synthesized *via* a simple method. Through various characterization techniques, it was concluded that the narrow band gap of the composite was due to the increased oxygen vacancies and the introduction of Ti^{3+} species. Compared to that of bare TiO_2(B) and ZIF-8, the degradation effect of the TiO_2(B)/ZIF-8-0.05 composite increased by 8 and 3.6 times, respectively. These results provide important clues for the semiconductor modification and coupling with metal–organic frameworks, which need to be continuously developed and applied in practice.

Conflicts of interest

There are no conflicts to declare.

Acknowledgements

The authors thank the financial support from Program for the Development of Science and Technology of Jilin Province (No. 20170204038GX).

References

1 B. Bajorowicz, M. P. Kobylanski, A. Golabiewska, J. Nadolna, A. Zaleska-Medynska and A. Malankowska, Quantum dot-decorated semiconductor micro- and nanoparticles: A review of their synthesis, characterization and application in photocatalysis, *Adv. Colloid Interface Sci.*, 2018, **256**, 352–372.

2 Y. Xu, C. Zhang, P. Lu, X. Zhang, L. Zhang and J. Shi, Overcoming poisoning effects of heavy metal ions against photocatalysis for synergetic photo-hydrogen generation from wastewater, *Nano Energy*, 2017, **38**, 494–503.

3 L. Shen, Z. Xing, J. Zou, Z. Li, X. Wu, Y. Zhang, Q. Zhu, S. Yang and W. Zhou, Black TiO_2 nanobelts/g-C_3N_4 nanosheets Laminated Heterojunctions with Efficient Visible-Light-Driven Photocatalytic Performance, *Sci. Rep.*, 2017, **7**, 41978.

4 J. Becker, K. R. Raghupathi, J. St. Pierre, D. Zhao and R. T. Koodali, Tuning of the Crystallite and Particle Sizes of ZnO Nanocrystalline Materials in Solvothermal Synthesis and Their Photocatalytic Activity for Dye Degradation, *J. Phys. Chem. C*, 2011, **115**(28), 13844–13850.

5 R. Zhang, B. Du, Q. Li, Z. Cao, G. Feng and X. Wang, α-Fe_2O_3 nanoclusters confined into UiO-66 for efficient visible-light photodegradation performance, *Appl. Surf. Sci.*, 2019, **466**, 956–963.

6 O. Sacco, V. Vaiano, D. Sannino, R. A. Picca and N. Cioffi, Ag modified ZnS for photocatalytic water pollutants degradation: Influence of metal loading and preparation method, *J. Colloid Interface Sci.*, 2019, **537**, 671–681.

7 R. Bera, S. Kundu and A. Patra, 2D Hybrid Nanostructure of Reduced Graphene Oxide–CdS Nanosheet for Enhanced Photocatalysis, *ACS Appl. Mater. Interfaces*, 2015, **7**(24), 13251–13259.

8 Q. Li, F. Wang, L. Sun, Z. Jiang, T. Ye, M. Chen, Q. Bai, C. Wang and X. Han, Design and Synthesis of Cu@CuS Yolk–Shell Structures with Enhanced Photocatalytic Activity, *Nano-Micro Lett.*, 2017, **9**(3), 35.

9 J. Fu, J. Yu, C. Jiang and B. Cheng, g-C3N4-Based Heterostructured Photocatalysts, *Adv. Energy Mater.*, 2018, **8**(3), 1701503.

10 N. F. F. Moreira, M. J. Sampaio, A. R. Ribeiro, C. G. Silva, J. L. Faria and A. M. T. Silva, Metal-free g-C_3N_4 photocatalysis of organic micropollutants in urban wastewater under visible light, *Appl. Catal., B*, 2019, **248**, 184–192.

11 B. Paik, M. Tsubota, T. Ichikawa and Y. Kojima, Catalytic effect of $ATiO_3$ (A = Sr, Ba) on ammonia decomposition during mechanical milling, *Chem. Commun.*, 2010, **46**(22), 3982–3984.

12 M. Wu, K. Fu, H. Deng and J. Shi, Cobalt tetracarboxyl phthalocyanine-manganese octahedral molecular sieve (OMS-2) as a heterogeneous catalyst of peroxymonosulfate for degradation of diclofenac, *Chemosphere*, 2019, **219**, 756–765.

13 S. Sharma, V. Dutta, P. Singh, P. Raizada, A. Rahmani-Sani, A. Hosseini-Bandegharaei and V. K. Thakur, Carbon quantum dot supported semiconductor photocatalysts for efficient degradation of organic pollutants in water: A review, *J. Cleaner Prod.*, 2019, **228**, 755–769.

14 M. Zhang, Q. Shang, Y. Wan, Q. Cheng, G. Liao and Z. Pan, Self-template synthesis of double-shell TiO_2@ZIF-8 hollow

nanospheres via sonocrystallization with enhanced photocatalytic activities in hydrogen generation, *Appl. Catal., B*, 2019, **241**, 149–158.

15 X. Wang, R. Xia, E. Muhire, S. Jiang, X. Huo and M. Gao, Highly enhanced photocatalytic performance of TiO2 nanosheets through constructing TiO2/TiO2 quantum dots homojunction, *Appl. Surf. Sci.*, 2018, **459**, 9–15.

16 A. S. Weber, A. M. Grady and R. T. Koodali, Lanthanide modified semiconductor photocatalysts, *Catal. Sci. Technol.*, 2012, **2**(4), 683–693.

17 X. Sun, J. Lin, H. Guan, L. Li, L. Sun, Y. Wang, S. Miao, Y. Su and X. Wang, Complete oxidation of formaldehyde over TiO_2 supported subnanometer Rh catalyst at ambient temperature, *Appl. Catal., B*, 2018, **226**, 575–584.

18 H. H. Mohamed and A. A. Alsanea, TiO_2/carbon dots decorated reduced graphene oxide composites from waste car bumper and TiO_2 nanoparticles for photocatalytic applications, *Arabian J. Chem.*, 2020, **13**, 3082–3091.

19 A. Giampiccolo, D. M. Tobaldi, S. G. Leonardi, B. J. Murdoch, M. P. Seabra, M. P. Ansell, G. Neri and R. J. Ball, Sol gel graphene/TiO_2 nanoparticles for the photocatalytic-assisted sensing and abatement of NO_2, *Appl. Catal., B*, 2019, **243**, 183–194.

20 J. Ye, J. He, S. Wang, X. Zhou, Y. Zhang, G. Liu and Y. Yang, Nickel-loaded black TiO_2 with inverse opal structure for photocatalytic reduction of CO_2 under visible light, *Sep. Purif. Technol.*, 2019, **220**, 8–15.

21 Y. Pi, X. Li, Q. Xia, J. Wu, Y. Li, J. Xiao and Z. Li, Adsorptive and photocatalytic removal of Persistent Organic Pollutants (POPs) in water by metal-organic frameworks (MOFs), *Chem. Eng. J.*, 2018, **337**, 351–371.

22 X. Gong, R. Zhao, J. Qin, H. Wang and D. Wang, Ultra-efficient removal of NO in a MOFs-NTP synergistic process at ambient temperature, *Chem. Eng. J.*, 2019, **358**, 291–298.

23 Y. Gao, J. Xia, D. Liu, R. Kang, G. Yu and S. Deng, Synthesis of mixed-linker Zr-MOFs for emerging contaminant adsorption and photodegradation under visible light, *Chem. Eng. J.*, 2019, **378**, 122118.

24 S. Li, P. Luo, H. Wu, C. Wei, Y. Hu and G. Qiu, Strategies for Improving the Performance and Application of MOFs Photocatalysts, *ChemCatChem*, 2019, **11**(13), 2978–2993.

25 D. Sun, P. R. Adiyala, S. J. Yim and D. P. Kim, Pore-Surface Engineering by Decorating Metal-Oxo Nodes with Phenylsilane to Give Versatile Super-Hydrophobic Metal-Organic Frameworks (MOFs), *Angew. Chem., Int. Ed.*, 2019, **58**(22), 7405–7409.

26 C. V. Reddy, K. R. Reddy, V. V. N. Harish, J. Shim, M. V. Shankar, N. P. Shetti and T. M. Aminabhavi, Metal-organic frameworks (MOFs)-based efficient heterogeneous photocatalysts: Synthesis, properties and its applications in photocatalytic hydrogen generation, CO_2 reduction and photodegradation of organic dyes, *Int. J. Hydrogen Energy*, 2020, **45**, 7656–7679.

27 X. Deng, Z. Li and H. Garcia, Visible Light Induced Organic Transformations Using Metal-Organic-Frameworks (MOFs), *Chemistry*, 2017, **23**(47), 11189–11209.

28 Z. Lei, Y. Xue, W. Chen, W. Qiu, Y. Zhang, S. Horike and L. Tang, MOFs-Based Heterogeneous Catalysts: New Opportunities for Energy-Related CO_2 Conversion, *Adv. Energy Mater.*, 2018, **8**(32), 1801587.

29 Y. Tang, D. Dubbeldam, X. Guo, G. Rothenberg and S. Tanase, Efficient Separation of Ethanol-Methanol and Ethanol-Water Mixtures Using ZIF-8 Supported on a Hierarchical Porous Mixed-Oxide Substrate, *ACS Appl. Mater. Interfaces*, 2019, **11**(23), 21126–21136.

30 L. Zhou, N. Li, G. Owens and Z. Chen, Simultaneous removal of mixed contaminants, copper and norfloxacin, from aqueous solution by ZIF-8, *Chem. Eng. J.*, 2019, **362**, 628–637.

31 Q. Li, W. Yang, F. Li, A. Cui and J. Hong, Preparation of CoB/ZIF-8 supported catalyst by single step reduction and its activity in hydrogen production, *Int. J. Hydrogen Energy*, 2018, **43**(1), 271–282.

32 E. Pipelzadeh, V. Rudolph, G. Hanson, C. Noble and L. Wang, Photoreduction of CO2 on ZIF-8/TiO2 nanocomposites in a gaseous photoreactor under pressure swing, *Appl. Catal., B*, 2017, **218**, 672–678.

33 X. Chen, L. Liu, P. Y. Yu and S. S. Mao, Increasing Solar Absorption for Photocatalysis with Black Hydrogenated Titanium Dioxide Nanocrystals, *Science*, 2011, **331**, 746–750.

34 G. Rajender, J. Kumar and P. K. Giri, Interfacial charge transfer in oxygen deficient TiO2-graphene quantum dot hybrid and its influence on the enhanced visible light photocatalysis, *Appl. Catal., B*, 2018, **224**, 960–972.

35 A. Balati, S. Tek, K. Nash and H. Shipley, Nanoarchitecture of TiO_2 microspheres with expanded lattice interlayers and its heterojunction to the laser modified black TiO_2 using pulsed laser ablation in liquid with improved photocatalytic performance under visible light irradiation, *J. Colloid Interface Sci.*, 2019, **541**, 234–248.

36 W. F. Zhang, Y. L. He, M. S. Zhang, Z. Yin and Q. Chen, Raman scattering study on anatase TiO2nanocrystals, *J. Phys. D: Appl. Phys.*, 2000, **33**(8), 912–916.

37 B. Santara, P. K. Giri, K. Imakita and M. Fujii, Evidence of oxygen vacancy induced room temperature ferromagnetism in solvothermally synthesized undoped TiO2 nanoribbons, *Nanoscale*, 2013, **5**(12), 5476–5488.

38 S. Umrao, S. Abraham, F. Theil, S. Pandey, V. Ciobota, P. K. Shukla, C. J. Rupp, S. Chakraborty, R. Ahuja, J. Popp, B. Dietzek and A. Srivastava, A possible mechanism for the emergence of an additional band gap due to a Ti–O–C bond in the TiO2–graphene hybrid system for enhanced photodegradation of methylene blue under visible light, *RSC Adv.*, 2014, **4**(104), 59890–59901.

39 Z.-W. Wu, S.-L. Tyan, H.-H. Chen, J.-C.-A. Huang, Y.-C. Huang, C.-R. Lee and T.-S. Mo, Temperature-dependent photoluminescence and XPS study of ZnO nanowires grown on flexible Zn foil via thermal oxidation, *Superlattices Microstruct.*, 2017, **107**, 38–43.

40 W. Fang, M. Xing and J. Zhang, A new approach to prepare Ti3+ self-doped TiO2 via NaBH4 reduction and hydrochloric acid treatment, *Appl. Catal., B*, 2014, **160–161**, 240–246.
41 C. Li, Q. Han, Y. Pan, J. Zhao, Y. Luo and P. Na, Insights into the photosensitization activity of zirconium-titanium pyrophosphate under visible light irradiation, *Mater. Lett.*, 2020, **268**, 127399.
42 W. Shi, F. Guo, H. Wang, M. Han, H. Li, S. Yuan, H. Huang, Y. Liu and Z. Kang, Carbon dots decorated the exposing high-reactive (111) facets CoO octahedrons with enhanced photocatalytic activity and stability for tetracycline degradation under visible light irradiation, *Appl. Catal., B*, 2017, **219**, 36–44.
43 J. Zheng and L. Zhang, Designing 3D magnetic peony flower-like cobalt oxides/g-C_3N_4 dual Z-scheme photocatalyst for remarkably enhanced sunlight driven photocatalytic redox activity, *Chem. Eng. J.*, 2019, **369**, 947–956.
44 Y. Matsumoto, Energy Positions of Oxide Semiconductors and Photocatalysis with Iron Complex Oxides, *J. Solid State Chem.*, 1996, **126**(2), 227–234.